1   **Methodological Considerations in Cover-Collapse Sinkhole**

2   **Analyses: A Case Study of Southeastern China's Guangzhou City**

3   Long Jia[a,b,c], Yan Meng[a,b,c], Lujuan Li[b], Renchao Yin[b,c],

4   [a]China University of Geosciences, Wuhan 430074,China

5   [b]Institute of Karst Geology, Chinese Academy of Geological Sciences, Guilin 541004, China

6   [c]Key Laboratory of Karst Collapse Prevention, CAGS, Guilin 541004, China

7   **Abstract**

8   Cover-collapse sinkholes can present significant hazards to human habitation and communal facilities

9   in soil-covered karst regions. Therefore, for human security and land-use planning in sinkhole-prone areas,

10   appropriate approaches are required prior to construction in order to understand the cover-collapse sinkhole

11   genesis and its likely evolution. The study seeks to contribute to performing an integrated analysis of karst

12   hazards in mantle karst regions where karst evidence can be masked, with the ultimate goal of developing a

13   methodological framework utilizing different techniques and approaches. A small area located in

14   Guangzhou City of southeastern China's Guangdong Province was analyzed. The detailed typology,

15   morphometry, and chronology inventory of 49 cover-collapse sinkholes in the study area were analyzed

16   using various surface investigation methods, such as field surveys, aerial photography, and

17   photogrammetry. The Quaternary deposits and indicators of the active underground karst features in the

18   aforementioned mantle karst region were geotechnically characterized using drilling and geophysical

19   techniques. These techniques included ground penetrating radar (GPR), electrical resistivity imaging (ERI),

20   natural source audio frequency magnetotellurics (NSAMT), and micro-tremors. During this study's

21   investigations, three karst fissure zones covered by Quaternary soil were observed using multiple

22   techniques. In addition, it was found that the groundwater dynamic monitoring data confirmed that the

23   sinkholes in the study area were closely related to changes in groundwater levels. Therefore, the efforts

24   which have been made to investigate and monitor the sinkhole development will be required to continue

25   into the immediate future.

26   **Keywords:** cover-collapse sinkholes; karst; geomorphological analyses; geophysical surveys

1. Introduction

28   As near-surface indicators of active karst features in soil-covered karst regions, cover-collapse

29   sinkholes are the result of the downward water-borne transportation of soil or other related material into

30   underlying voids in either limestone bedrock or other soil profiles. Cover-collapse sinkholes are

31   characterized by roughly circular outlines, internal drainage, and distinct breaks in the land surface *(Tharp,*

32   *1999, 2002)*. Cover-collapse sinkholes are known to occur in many regions of the world *(Galve et al., 2015;*

33   *Zhou and Lei, 2017)*, and have caused serious damages to urban and industrial areas, as well as farming

34   regions. Therefore, due to the large and increasing impacts of sinkhole damages, including the loss of

35   human lives, various techniques and approaches focusing on the reconstruction of cover-collapse sinkhole

36   conditions have received increasing attention *(Kaufmann et al., 2018; Pueyo Anchuela et al., 2015; Zini et*

37   *al., 2015)*. These techniques and approaches can be divided into the following categories:

38   **(1)** *Field and photogrammetric surveys*: These surveys include historical satellite remote sensing

39   images, aerial photograph interpretations, and field surveys, which are often useful to analyze the

40   morphometry and chronology of cover-collapse sinkholes *(Al-Halbouni et al., 2017; Gutiérrez et al., 2007);*.

41   **(2)** *Non-invasive geophysical techniques*:

42   Subsurface cavities and the processes that lead to the development of sinkholes cause changes within

43   the subsurface, such as porosity, fracture density, and water saturation *(Frumkin et al., 2011)*. Before

44   collapse, non-invasive geophysical approaches may detect these changes, and include various techniques

45   such as microgravity *(Debeglia et al., 2006; Eppelbaum et al., 2008; Paine et al., 2012)*; micro-tremors

46   *(Maresca and Berrino, 2016)*; electrical resistivity tomography *(Ahmed and Carpenter, 2003; Gutiérrez et*

47   *al., 2019)*; seismic reflections *(Wadas et al., 2017)*; and electromagnetic surveys including GPR *(Ronen et*

48   *al., 2019).*

49   **(3) *Invasive techniques***: Invasive techniques include trenching *(Gutiérrez et al., 2009)*; drilling *(Cueto*

50   *et al., 2018)*; and geophysical well logging. Trenching and drilling processes are able to provide immediate

51   information on the nature and geotechnical properties of underground areas. Geophysical well logging can

52   contribute to filling the significant gaps which drilling processes and non-invasive geophysical methods

53   are unable to address.

54   **(4) *Monitoring***: Hydrogeological monitoring *(Jiang et al., 2019)* and ground deformation monitoring

55   *(Galve et al., 2015)* are commonly crucial aspects for understanding the causes of deformations, and are

56   adopted to assess and predict the kinematics of the subsidence phenomena. In particular, these monitoring

57   methods are necessary in cases of potential episodes of catastrophic collapse.

58   Karstic terrain is one of the most difficult natural geological hazards to assess for development and

59   construction unless proper measures are taken *(Xeidakis et al., 2004)*. Due to the high vertical and lateral

60   variabilities of the geological and hydrogeological characteristics in the karst regions, no single technique

61   has been found which can effectively resolve the related problems. Therefore, in the present study, a small

62   rigion with surface deformation issues located in southeastern China's Guangzhou City was examined for

63   the purpose of developing a methodological framework for the evaluations of the potential conditioning

64   factors which control the occurrences of sinkholes in soil-covered karst regions where karst evidence may

65   be hidden.

2. Geological setting

66

67
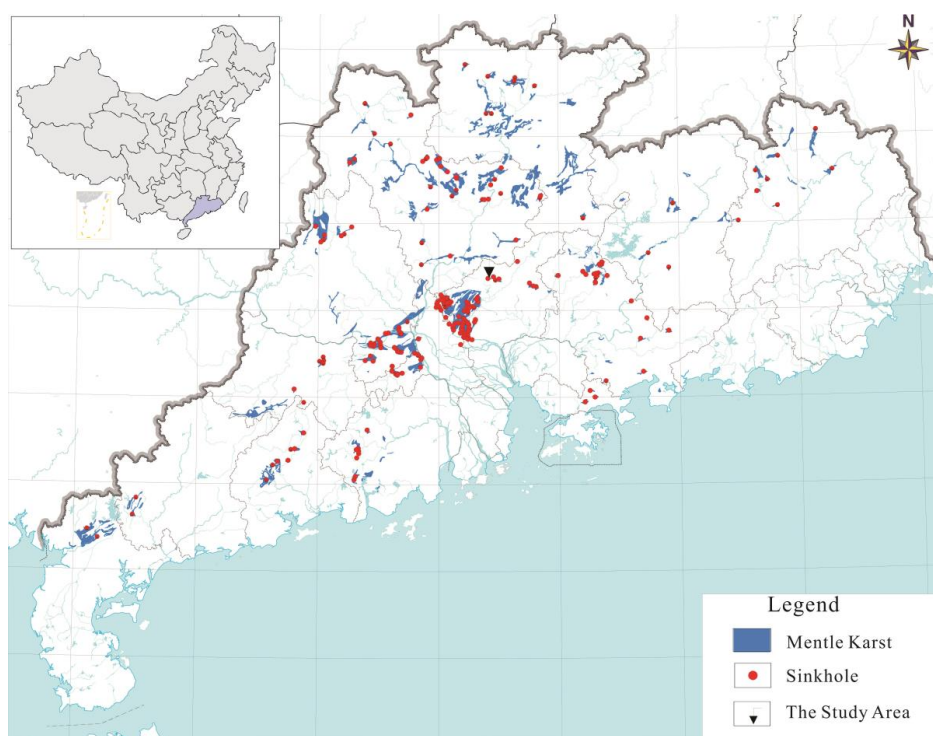
Figure 1. Karst sinkhole (affecting more than 100 people) distributions in China's Guangdong Province

69   From a geographical perspective, the study area was located in the central sector of the Pearl River

70   Delta, in Conghua District of Guangzhou City, Guangdong Province, in the southeastern region of China.

71   The geologic hazards related to cover-collapse sinkholes have occurred frequently in China's Guangdong

72   Province in recent years. As shown in Fig. 1, according to the statistical data, there were more than 400

73   large-scale karst cover-collapse sinkholes (affecting more than 100 people) in Guangdong Province.

74   The elevations in the study area had varied between 30 and 80 m above sea level, as shown in Fig. 2.

75   Quaternary deposits were observed to mantle the vast majority of the Carboniferous limestone. These

76   consisted of alluvial deposits with thick layers (4.65 to 13.8 m) of loose soil (China Geological Map,

77   F-49-24-A Conghua, Scale 1:50.000). The karst processes in the region were determined to be related to

78   the dissolution of Miocene Carbonate material, mainly covered by Quaternary material. In addition,

Natural Hazards
and Earth System
Sciences
Discussions

79   Jurassic volcanic strata and carboniferous sandstone strata were also distributed in the study area. The

80   evolution processes of the sinkholes appeared to be structurally controlled by the characteristics of the

81   local and regional faulting. The most important tectonic feature in the area was the "Guangzhou-Conghua"

82   fracture (which was buried within the study area and recognizable only inpart) with a typically $60\,°$NW

83   orientation. Generally speaking, a large part of the investigated area was occupied by paddy fields, and

84   buildings were relatively scarce. The cover-collapse sinkholes were evidenced in the alluvial plane of the

85   study area.
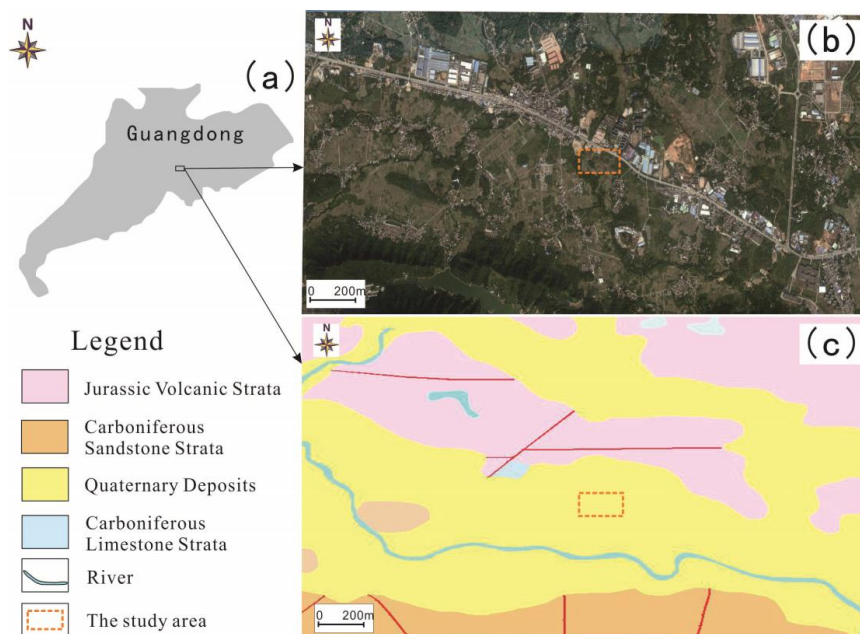
86
87   **Figure 2.** Geological and geomorphological setting of the study area: (a) Location of the study area in Guangdong Province
88   of southeastern China; (b) ©Google Earth image showing the study sites. The study sites as mapped by the authors are shown
89   (red rectangle); (c) Synthetic exposed stratigraphic map

90   **3. Methodology**

91   In order to understand the causes of the deformations, including sudden catastrophic collapses, as well

92   as accurately predict the kinematics of the subsidence phenomena in the study area, multidisciplinary

93   approaches were planned for the following purposes: 1. To ascertain the surface subsidence and sinkhole

94   features; 2. To precisely locate and define the subsurface karst features at depth, such as cavities, conduits,

95   and karst fissure zones; 3. To detect the thicknesses and stratification of soil and underlying subsidence

96   features; and 4. To monitor groundwater dynamic conditions and deformations.

97   **3.1 Surface investigations**

98   3.1.1 Field survey, documentary information and oral information

99   During the initial phase of this study's investigation, information data related to the selected sinkhole

100   areas which had been obtained from written documents, such as local maps or reports from public

101   institutions, were collected and analyzed in order to gain a good understanding of cover-collapse sinkhole

102   context. For example, previous cartographic production data were utilized, such as a local 1:50,000 scale

103   geological map. Also, the available rough information regarding the alluvium thickness, ground elevations,

104   and formation lithology were used in this study. During the investigation process, detailed field surveys

105   annotating 1:1000 scale color telephotographs were carried out in the selected sinkhole areas. In addition,

106   information from local residents was found to substantially enrich the investigation content by providing

107   data on the spatial and temporal distributions of undetected and filled sinkholes, along with the weather

108   conditions and well water level changes at that time.

109   **3.1.2 Aerial photogrammetry and historical satellite remote sensing images**

110   In aerial photogrammetry, unmanned aerial vehicle (UAV) platforms can be used to capture digital

111   surface and terrain models for large scale mapping, with an accuracy down to the cm-level from various

112   waypoints in investigated regions *(Chiabrando et al., 2011; Lee et al., 2016; Yeh et al., 2016)*. In the present

113   study, detailed and accurate geomorphological data including surface elevation of the study area were

114   provided by senseFly mapping drones using Postflight Terra 3D software. Also, historical images available

115   from Google Earth were used to obtain information on the recent morphological changes of the analyzed

116   sinkholes in the study area. The detailed interpretations of photographs taken on different dates

117   (2014/10/28; 2015/12/05) assisted in this study's analysis of the spatio-temporal distribution patterns of the

118 subsidence phenomena.

119 **3.2 Non-intrusive geophysical prospecting**

120 **3.2.1 Surface-based GPR**

121 Ground Penetrating Radar (GPR) surveys are a type of geophysical technique which offer a very high

122 resolution abilities in order to locate and characterize the sedimentological information of subsoil (such as

123 soil-cavities and the presence of active subsidence, and so on) *(Anchuela et al., 2009; Chalikakis et al.,*

124 *2011; Lei et al., 2008).* In GPR profiles, information can be identified by changes in color, which are

125 related to the amplitude of the recorded wave at each point. However, this technique has been found to

126 have its own shortcomings, due to the fact that the depths of surface-based GPR detections were generally

127 found to be only 3 to 5 m in southern China. In the present study, 20 surface-based GPR (Ground

128 Penetrating Radar) profiles with a total length of 3 km were conducted in the study area, as detailed in Fig.

129 2. The continuous GPR profiles were collected utilizing a SIR3000 GPR instrument manufactured by the

130 Geophysical Survey System Inc. (GSSI) in the United States, equiped with a 100 MHz bowtie bistatic

131 antenna.

132 **3.2.2 Micro-tremors**

133 Micro-tremors are passive source vibration signals which originate from natural or human activities.

134 These vibration signals carry abundant information regarding underground geological structures. The

135 Nakamura technique of microtremor exploration, also known as the H/V ratio method, is a widely used

136 passive seismic technique by researchers for obtaining overburden sedimentary layer thicknesses *(Dinesh*

137 *et al., 2010).* With this technique, the calibration relationships between the soil thicknesses and the

138 prominent resonant frequencies in the H/V spectrum are obtained from borehole drilling logs. Therefore,

139 the resonant frequencies can be used to obtain the thicknesses of the sediment in the area near the borehole.

140 In this study, single-station micro-tremor data came from a Tromino 3G seismograph were collected from

141   the 318 sites. The sites were spaced 5 m apart, and the single point collection time was 20 minutes.

3.2.3 Electrical resistivity imaging (ERI)

143   Electrical resistivity imaging (ERI) is a technique in which many individual resistivity measurements

144   are combined to produce a resistivity cross-section of the subsurface. Electrical parameters, such as

145   resistivity or conductivity, are very sensitive to formation properties. Therefore, ERI methods have been

146   effectively used for differentiation processes related to rock layers. Electrical resistivity tomography

147   profiling (surface electrode arrays) is also commonly used for sinkhole investigations as a means of

148   identifying shallow limestone deposits, large dissolution feature zones, and underlying cavities *(Fabregat*

149   *et al., 2017)*. In the present study, two ERI (electrical resistivity image) profiles, with a total length of 500

150   m and spacing of 30 m, were conducted in the study area. The resistivity lines of this pattern were acquired

151   utilizing a WDJD-3 Supersting multi-channel and multi-electrode resistivity system designed in China,

152   equipped with 60 electrodes spaced at 5 m intervals along each line. The data were inverted using

153   RES2DINV software.

3.2.4 Natural source audio frequency magnetotellurics (NSAMT)

155   Audio frequency magnetotelluric (AMT) methods involve surface-based electromagnetic sounding

156   techniques which use fixed grounded dipoles as signal sources (CSAMT), or alternatively, the

157   naturally-occurring fields of the Earth's atmospheric system (NSAMT). The higher frequency

158   audio-magnetotelluric (AMT) methods are able to detect the ranges of karst fissure zones based on the

159   different electrical conductivity of the underground rock strata. Once water flows into caved and fractured

160   zones, the resistivity of those areas will rapidly decrease. These are referred to as low-resistivity anomaly

161   zones. In this study, the naturally-occurring electromagnetic fields were used as the signal sources. Then,

162   NSAMT (Natural Source Audio Frequency Magnetotelluric) profiles with total lengths of 500 m were

163   conducted in the areas coinciding with the ERI profiles. The NSAMT data were collected using a

164   Geometrics StrataGem EH4 system in the study area. Then, an EH-4 conductivity imaging system

165   manufactured by EMI and Geometrics (US), was adopted in this study as the electromagnetic geophysical

166   detection system for the auto data acquisition and processing procedures.

167   **3.3 Intrusive techniques**

168   **3.3.1 Drilling**

169   Drilling processes provide valuable information on the nature and geotechnical properties of

170   underground areas and assists in the recognition of voids (including soil caves, karst caves, and karst

171   conduits) and sediment (disturbed by subsidence processes). Six boreholes were arranged in a selected

172   sector of Bumei Village, with a total footage of 407 m, which were referred to as the drilled cores.

173   **3.3.2 Single-hole radar**

174   Single-hole radar techniques are commonly utilized to record single-hole full-waveform radar data.

175   These data can potentially supply information on the nature of the reflectors distributed along the

176   boreholes *(Kim et al., 2007)*. A fixed-offset transmitter- and receiver-antennae pair were pulled slowly up

177   the length of a borehole during the single-hole radar detection process. The principle of the single-hole

178   reflection method is similar to that of surface-based GPR, with the exception that reflectors may occur on

179   all sides of the borehole recording line. Planar features, such as fault surfaces, which may be intersected by

180   a borehole, will appear as V-shaped reflections in a single-hole radar section. The images of the point

181   reflectors (for example, karst caves) are hyperbola. In the current study, a MALA system equipped with

182   100 MHz borehole antennae was used to acquire all of the radar data. The single-hole full-waveform data

183   were recorded in all six holes utilizing transmitter and receiver antennae separated by 2.75 m.

184   **3.3.3 Cross-hole radar**

185   Cross-hole GPR is a trans-illumination survey method in which two antennae are lowered down into

186   adjacent parallel boreholes *(Bachrach et al., 2005; Cordua et al., 2009)*. Then, by transmitting radar signals

187 from one borehole to another, the electromagnetic EM wave velocity and attenuation between the two

188 boreholes can be estimated. The high-resolution imaging of subsurface electromagnetic EM wave

189 velocities has proven to be effective in detections conducted in the majority of water-filled areas, such as

190 water-filled faults and caves, in which the low-speed zones represent the water filled areas *(Tan et al.,*

191 *2012)*. In this study, three pairs of boreholes were used for cross-hole radar surveys, taking advantage of

192 the adopted MALA system with 100 MHz borehole antennae.

193 **3.4 Monitoring methodologies**

194 3.4.1 Hydro-dynamic monitoring

195 　In many parts of the world (including China), recent research reports have revealed that a major

196 proportion of recent cover-collapse sinkhole events have been induced by anthropogenic changes in

197 hydrogeological systems *(Anikeev, 1999; Lei et al., 2016; Meng et al., 2014)*. Therefore, the monitoring of

198 groundwater levels may become an effective method for capturing real-time changes in the underground

199 hydrodynamic forces, and possibly even used to forecast the appearances of cover-collapse sinkholes. In

200 the study area, the water levels in two of the boreholes had been monitored since January of 2015. The

201 monitoring intervals were 20 minutes.

202 **3.4.2 InSAR**

203 　Interferometric Synthetic Aperture Radar (InSAR) analysis methods can be used to screen large areas

204 for anomalous vertical movements, as well as to guide intensive field investigations and detection

205 processes to areas where significant changes are occurring *(Intrieri et al., 2015)*. In addition, the mapping

206 of ground displacements may assist in the identification of locations prone to future cover-collapse

207 sinkholes. In the study area, InSAR ground deformation data were obtained with a 5 m pixel size and a

208 vertical accuracy higher than 3 m. Then, three RADARSAT-2 Ultra Fine images from November 27th of

209 2015, January 14th of 2016, and March 2nd of 2016 were selected for further examination.

Natural Hazards
and Earth System
Sciences
Discussions
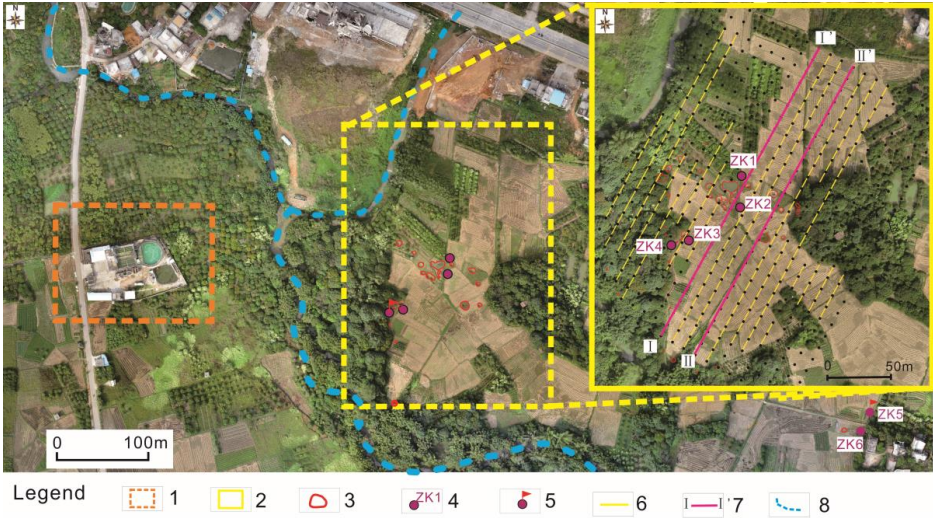
Figure 3. Investigation layout of the research area (Background image from aerial photograph provided by the authors' senseFly mapping drone): 1. Waterworks; 2. Research areas; 3. Sinkhole pits; 4. Boreholes; 5. Groundwater level monitoring points; 6. Ground penetrating radar lines; 7. Geophysical detection lines (GPR, ERI, and AMT); 8. Brook area

4. Results

4.1 Sinkhole inventory

The field surveys with drones aerial photogrammetry, along with the historical satellite remote sensing images, had assisted in the mapping of the sinkhole detailed inventory to be accomplished, as shown in Fig. 3, Fig. 4b and Fig. 5a. There were 49 cover-collapse sinkholes observed in the selected area. Table 1 presents the morphometry and chronology of the inventoried sinkholes. These collapses, which had resulted in direct economic losses, had mainly occurred between September of 2014 and March of 2015. The Google Earth images from prior to 2014 showed no sinkholes in the area. In addition, 47 collapse pits were identified in the aerial photographs from 2014 to 2015. Two more sinkholes had formed in the area in October of 2016 and March of 2017, respectively. No casualties had resulted from the sinkhole collapses. However, a portion of the rice harvest was lost and some of the fruit trees in the area were destroyed.

229
230

Table 1 The dimensions and dates of sinkholes

ID	Shape	Diameter or Major axis/ Minor axis	Major axis direction	Date and time	Depth	ID	Shape	Diameter or Major axis/ Minor axis	Major axis direction	Date and time	Depth
1	Circle	2.8		Sep-14	0.9	25	Ellipse	0.9/0.6	0	Sep-14	0.5
2	Circle	7.8		Sep-14	0.8	26	Circle	1.7		Sep-14	1
3	Circle	3.1		Jun-14	0.9	27	Ellipse	1.8/0.9	120	Sep-14	1
4	Circle	4.9		Sep-14	1	28	Circle	3.3		Sep-14	1
5	Circle	3.2		Sep-14	1	29	Ellipse	1.3/1		Sep-14	0.98
6	Ellipse	13.4/7.2		Sep-14	1.2	30	Ellipse	2.2/1.5	205	Oct-14	1
7	Circle	2.6		Sep-14	2	31	Circle	2.6/1.8	345	Oct-14	0.9
8	Circle	3.2		Sep-14	1.5	32	Circle	1		Sep-14	1
9	Circle	4.5		Sep-14	0.8	33	Ellipse	2.1/1.3	280	Jan-15	1.5
10	Circle	4.8		Sep-14	0.9	34	Ellipse	3.7		Dec-14	2
11	Circle	1.8		Sep-14	0.8	35	Ellipse	8/6		Sep-14	1
12	Circle	2.4		Sep-14	0.9	36	Ellipse	12/6		Nov-14	2.2
13	Circle	2.3		Sep-14	1	37	Circle	1.8		Nov-14	0.4
14	Circle	4.0		Sep-14	0.8	38	Ellipse	2.8/1.2	40	Mar-15	1
15	Circle	3.2		Sep-14	1.5	39	Circle	1.9		Mar-15	1.35
16	Circle	1.8		Sep-14	1.5	40	Circle	1.8		Nov-14	0.7
17	Ellipse	4.6/3.8	290	Sep-14	1.3	41	Circle	1.7		Nov-14	0.7
18	Circle	2.1		Sep-14	0.75	42	Circle	2.4		Nov-14	1.1
19	Ellipse	2.4/2	85	Sep-14	0.7	43	Ellipse	1.3/0.5	0	Nov-14	0.7
20	Ellipse	2.2/1.9	45	Sep-14	0.38	44	Ellipse	1.2/0.8	10	Nov-14	2
21	Ellipse	2/1.2	115	Sep-14	1.5	45	Circle	1.1/0.5	10	Nov-14	0.2
22	Circle	1.6		Sep-14	1.6	46	Circle	1.5		Nov-14	0.5
23	Ellipse	9.5/7.0	280	Sep-14	2	47	Circle	8.5		Nov-14	1.4
24	Ellipse	13/7	7	Sep-14	2	48	Circle	2.1		Oct-14	0.8
						49	Circle	2		Nov-16	0.9

231
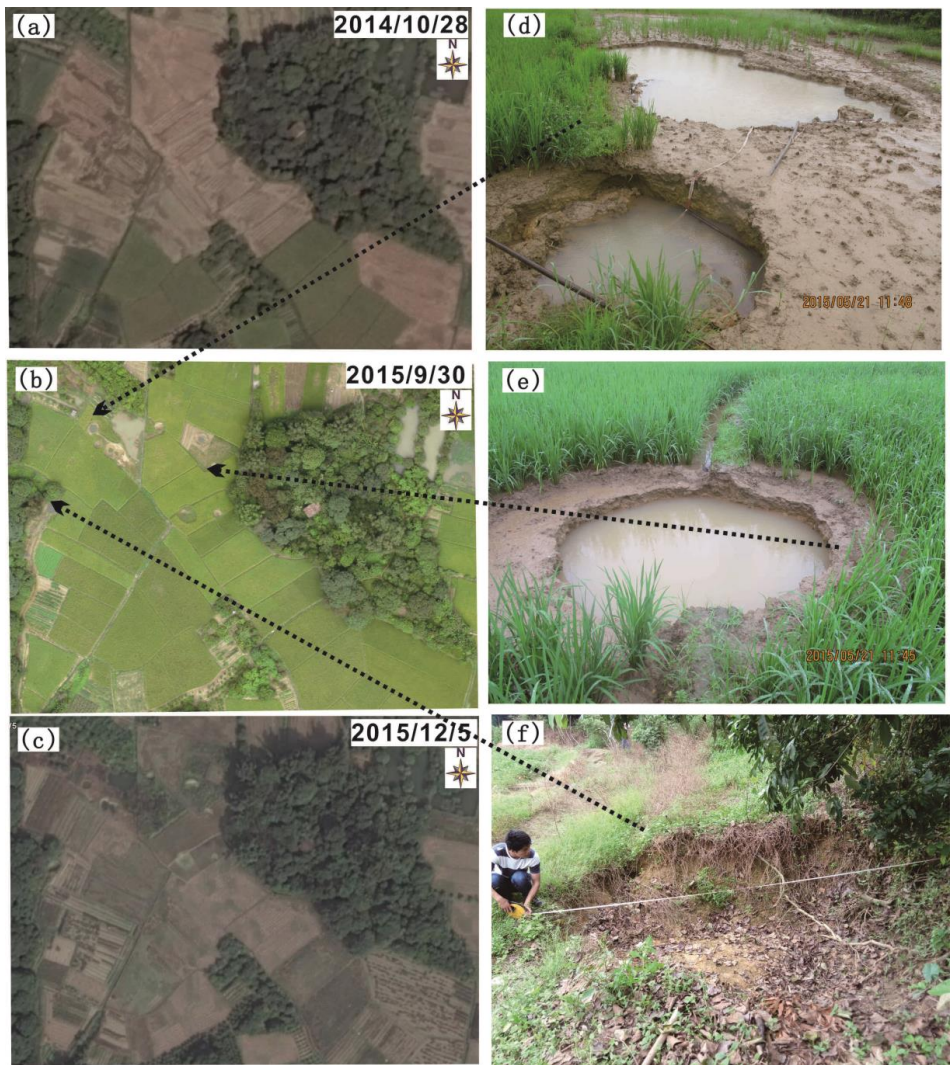
Figure 4. Sinkhole images in the research area: (a) and (c) ©Google Earth image showing the study site on October 28, 2014 and December 5, 2015; (b) Aerial photograph provided by the authors' senseFly mapping drone on September 30, 2015; (d), (e), and (f) Sinkhole camera photos

4.2 Soil layers

The thicknesses and structures of the soil layers in the study area were obtained according to the

results of the drilling, micro-tremors, and electrical resistivity imaging (ERI).

4.2.1 Quaternary soil thicknesses

The drilling profiles showed that the thicknesses of the quaternary soil layers in the collapsed

Natural Hazards
and Earth System
Sciences
Discussions

242   intensive area ranged between 9 and 14.2 m in Fig. 7. In order to obtain a comprehensive understanding of

243   the Quaternary soil thicknesses in the study area, a contour map of the buried depths of the ground bedrock

244   was obtained by utilizing a micro-motion inversion method in Fig. 5b. In the southwestern area of the site,

245   the bedrock was determined to be between 12 and 15 m in depth. In the other areas of the site, the

246   thicknesses of the soil layers averaged approximately 10 m. The majority of the collapses had occurred in

247   the areas where the depths of bedrock had varied greatly.

248   **4.2.2 Quaternary soil structure**

249   The borehole dates had revealed that the structures of the soil layers changed greatly, as detailed in

250   Fig. 7. As determined from the drilling profiles, from the bottom to the top in the figure, the stratigraphy of

251   the area was characterized by the following: (1) Paleozoic carboniferous Shitengzi formations (C_1s,

252   limestone); (2) Quaternary alluvial layers (Qal, sand) or residual soil layers (Qel, clay); and (3) Planting

253   soil layers (Qpd). The two obtained ERI profiles in Fig. 6b and 6e revealed a high resistivity zone in the

254   southern surface of the study area. In addition, when combined with the results of this study's field

255   investigations, it was confirmed that there was a high resistance zone in Quaternary alluvial layers (Qal,

256   sand). There was also a low resistivity zone in Fig. 6b and 6e indentified on the northern surface of the

257   study area, which represented the Quaternary residual soil layers (Qel, clay) distribution area.

258   **4.3 Karst features**

259   Karst caves were discovered in four out of a total of 6 boreholes, and were considered to be the most

260   direct evidence of karst activities in the study ara. In addition, other karst caves and fissures around the

261   boreholes were discovered using geological borehole radar. It was found that, based on the transmission

262   time imaging of the cross-hole radar, a karst cave with an elevation of between 3 and 9 m existed between

263   drilling boreholes ZK1 and ZK2. Also, between drilling boreholes ZK5 and ZK6, the radar signal

264   low-speed zones represented water-filled karst caves and fissures in Fig. 7. Furthermore, the results of the

265   single-hole radar measurements showed that there were linear anomalies located around boreholes ZK1,

266   ZK5 and ZK6, indicating the existence of karst cracks in those areas.

267   As indiated in L1, L2 and L3 of Fig. 6, three low-resistivity anomaly zones revealed fault zone

268   structures in the overburden karst area sites, as identified in the ERI and EH4 profiles. The micro-tremor

269   detection data showed that the bedrock surfaces fluctuated greatly in the southwestern section of the study

270   area in Fig. 5. These findings were found to be consistent with the abnormal positions revealed in the ERI

271   and EH4 profiles. Furthermore, these results had indicated the specific locations and morphology of the

272   karst fracture zones.

273   In the present investigation, no soil caves were found in the survey line by surface-based GPR in Figs.

274   6a and 6d, which was consistent with the fact that no collapses had occurred in the survey area. The

275   disturbed and loose areas in the Quaternary overburden were delineated by surface-based GPR at a

276   position of 70 to 120 m in profile Ⅰ-Ⅰ' and at 40 to 100 m in profile Ⅱ-Ⅱ', excluding the disturbance

277   data.

278
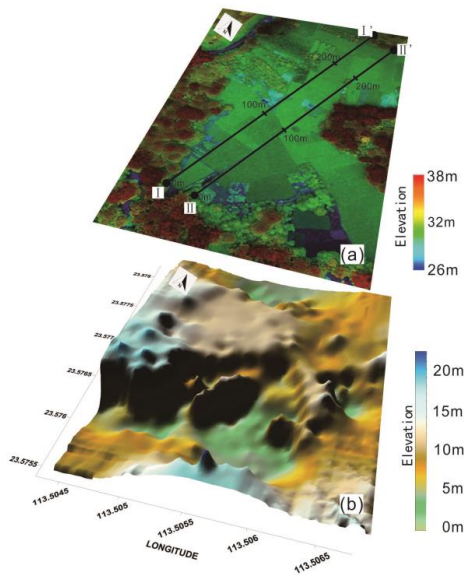
279
280 **Figure 5.** Geomorphological map and bedrock elevation map: (a) geomorphological map including surface elevation from
281 the authors' senseFly mapping drone; (b) Bedrock elevation map was obtained by utilizing a micro-motion inversion method.
282 Ⅰ-Ⅰ', Ⅱ-Ⅱ': Geophysical profile line
283
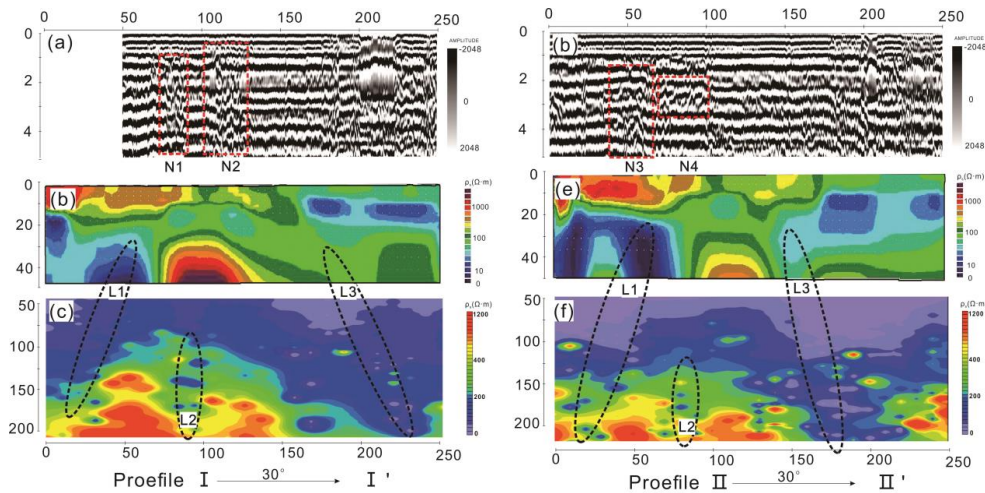
284
285 **Figure 6.** Geophysical interpretations of profiles: (a) Interpreted GPR section of profile Ⅰ-Ⅰ'; (b) Interpreted ERI section of
286 profile Ⅰ-Ⅰ'; (c) Interpreted NSAMT section of profile Ⅰ-Ⅰ'; (d) Interpreted GPR section of profile Ⅱ-Ⅱ'; (e)
287 Interpreted ERI section of profile Ⅱ-Ⅱ'; (f) Interpreted NSAMT section of profile Ⅱ-Ⅱ'; L1, L2, and L3 revealing the
288 low-resistivity anomaly zones; N1 to N4 refer to the disturbed and loose zones, respectively
289
290
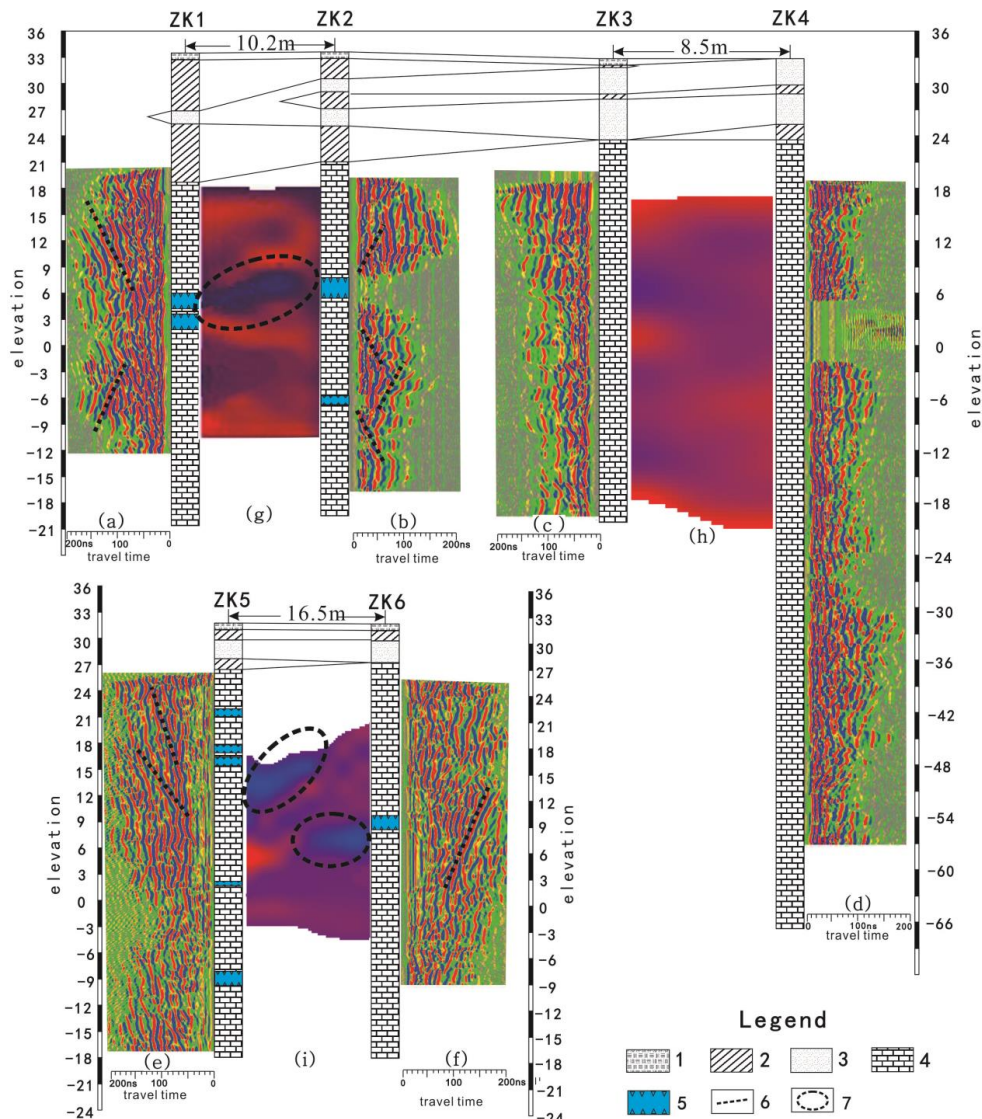
Figure 7. Borehole histogram and borehole radar images. (a) to (f) show the single-hole radar reflection images in which ZK1 to ZK6 show the borehole histogram; (g) to (i) are the cross-hole radar transillumination images: 1. Planting soil layers; 2. Quaternary residual soil layers (clay); 3. Quaternary alluvial soil layers (sand); 4. Paleozoic Carboniferous limestone; 5. Karst cave; 6. Karst fissures; 7. Low-speed zones representing the water filled areas

4.4 Changes in groundwater levels

In accordance with the information obtained from the local residents and staff, the daily water output of a waterworks located 800 m east of the study area was approximately 1,200 to 6,000 m^3. The change of water output was related to the water consumption of the residents. the water levels of the local wells had

301 dropped by about 7 m in early 2015 when a large scale karst collapse had occurred in the study area. Also,

302 on the basis of the hydrodynamic monitoring data, it was confirmed that there was a relationship between

303 groundwater level changes and the aforementioned collapse in the study area, as shown in Fig. 8. In

304 additon, the water table in the study area had experienced an approximate 8 m drop during the period

305 ranging from October of 2016 to December of 2017. It had been recorded that during this same period, two

306 new cover-collapse sinkholes had formed. However, since August of 2018, the groundwater levels have

307 recovered, and no further karst collapses have occurred in the study area.
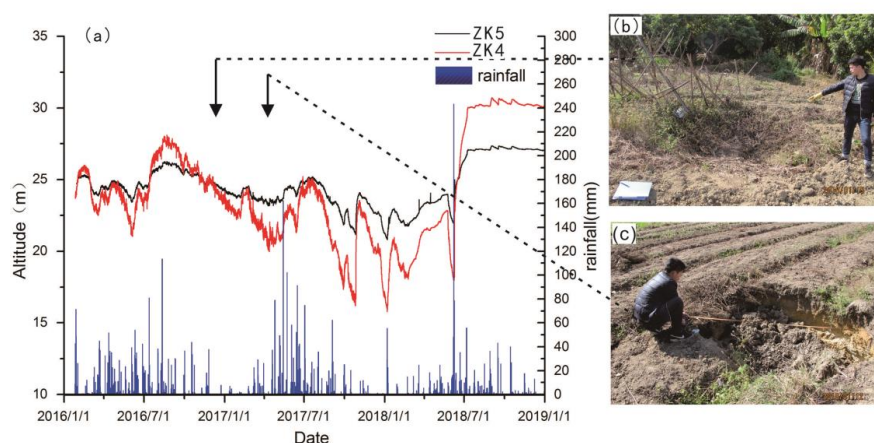
308
309 **Figure 8.** Hydrodynamic monitoring data and cover-collapse sinkholes: (A) Hydrodynamic monitoring data of drilling
310 boreshole ZK5 and drilling borehole ZK4; (B) Image of the cover-collapse sinkhole ID 48; (C) Image of the cover-collapse
311 sinkhole ID 49
312
313 **4.5 Ground deformations**

314 It was determined in this study that large-sized ground deformations did not exist in the study area, as

315 evidenced by the combined results of the three examined RADARSAT-2 Ultra Fine images taken on

316 November 27th of 2015, January 14th of 2016, and March 2nd of 2016. The InSAR ground deformation data

317 indicated a temporary steady-state in the study area following the occurrences of large-scale sinkhole

318 geological hazards.

5. Discussion

In accordance with surveys in China, the analysis processes for cover-collapse sinkhole conditions should involve three main steps, with each step built upon the previous one, as follows:

5.1 Geomorphic analysis

This study illustrated that geomorphic mapping which utilizes historical aerial photographs and unmanned aerial vehicle (UAV) images may be essential for investigations of cover-collapse sinkholes. The UAV images were found to have advantages over the satellite images, due to the fact that they had captured aerial images from certain flying heights with flexible flying missions and time frames. However, the effectiveness of the aforementioned approach may be quite limited in areas where the geomorphic expressions of sinkholes have been obliterated by natural processes or anthropogenic fill. Therefore, on this basis, thorough reconnaissance of the ground would be required to locate sinkholes not identifiable on aerial photographs due to high vegetation cover. It was also determined that information from local residents in the area was conducive to ascertaining the precise spatial distributions of the complex sinkhole clusters, especially concealed sinkholes which may be masked by anthropic landforms. One of the meaningful aspects of this case study was that the geomorphic model produced by combining data from aerial photographs and field surveys could potentially constitute a basis for accurately designing future site investigations and interpreting the results, such as implementing geophysical profiles and borehole data.

5.2 Geological analysis

Due to the complex and sometimes chaotic underlying geology observed in mantle karst areas, investigations which combine several methods are generally the only way to achieve satisfactory geological models for such areas.

Borehole drilling processes are performed in mantle karst regions in order to geotechnically characterize the stratigraphic information and calibrate and validate the geophysical detection results.

Natural Hazards
and Earth System
Sciences
Discussions

Open Access

EGU

342   However, drilling activities are expensive and time-consuming techniques, and the limited drill footage

343   may potentially have a high degree of uncertainty for the complex underlying geology in karst areas.

344   However, the punctual information derived from limited numbers of boreholes could be extended

345   laterally using borehole geophysical investigations, such as single-hole radar and cross-hole radar. In this

346   way, other karst caves and fissures around the borehole clouds may be discovered using geological

347   borehole radar techniques.

348   In the present study, based on the limited borehole data, micro-tremor explorations were used to

349   estimate the sediment thicknesses, thereby making it possible to reconstruct the bedrock morphology

350   beneath the entire study area. The non-disturbed areas were represented by the general horizontal bedding

351   of the Quaternary deposits. Therefore, any local thinning or thickening of the Quaternary deposits observed

352   using the mirco-tremor Nakamura technique were believed to indicate the presence of serial sediment

353   within active karst areas.

354   In addition, the ERI and NSAMT profiles had revealed imaging shallow fault zone structures at the

355   overburden karst area sites. The NSAMT sections were found to have poor measurement effects in the

356   range of 0 to 50 m, and good exploration effects in the range of 50 to 200 m. Meanwhile, the ERI sections

357   had satisfactorily imaged the general geometry of the karst structures in the range of 0 to 50 m. The

358   subsurface cavities and deformation structure clouds were detectable with the GPR, but only up to a

359   limited depth range of 2 to 5 m.

360   In the present study, the aforementioned techniques were examined in order to determine the most

361   advantageous synergistic approach in the study area. It was expected that the limitations observed in each

362   examined method would be balanced out by the advantages observed in the other methods.

Natural Hazards
and Earth System
Sciences
Discussions

EGU

363 **5.3 Dynamic monitoring**

364   In order to understand the causes of cover-collapse sinkholes, and to assess and predict the kinematics

365 of the subsidence phenomena, it is generally considered that monitoring methods are necessary. Since karst

366 cover-collapse sinkholes are known to be caused by declines in groundwater levels, a sound knowledge of

367 the short- and long-term dynamics of the effected hydrogeological systems are essential for sinkhole

368 hazard assessments. Hydrodynamic monitoring methods focus on the potential relationships between

369 hydrological changes and the development of cover-collapse sinkholes. The interpretations of the

370 groundwater level monitoring data allow the hydrogeological behaviors of the groundwater to be

371 accurately reconstructed. As a result, the kinematics of the subsidence phenomena can be assessed. In

372 addition, the accurate mapping of ground displacements may serve to identify the locations of future

373 cover-collapse sinkholes and guide future intensive field investigations. Therefore, it was found in this

374 study that monitoring of ground anomalous vertical movements by Interferometric Synthetic Aperture

375 Radar (InSAR) analysis could be an effective approach.

376 # 6. Conclusions

377   (1) In mantle karst regions, cover-collapse sinkholes are considered to be major geohazards due to the

378 large and increasing impacts of sinkhole damages. In this study, based on an appropriate methodological

379 framework, it was found that sinkhole condition analyses were conducive to human security and land-use

380 planning in sinkhole-prone areas.

381   (2) The multi-disciplinary approach adopted in this study was determined to the most effective

382 method for identifying and understanding cover-collapse sinkhole phenomena in a complex geological

383 frameworks, such as southeastern China's Bumei Village in the presented case study. The present study's

384 goal was to contribute to deepening the understanding the genesis and early-stage evolution of a sinkholes

Natural Hazards
and Earth System
Sciences

Open Access

EGU

Discussions

385   by utilizing geological, geomorphological, and hydrodynamic integrated methodologies. Special focus was

386   paid to the contributions of the various examined methods to overcome the limitations of the other

387   methods.

388   In this case study, a mapping procedure was introduced which combined data from aerial photographs

389   and intensive field investigations. The results clearly indicated the characterization of the cover-collapse

390   sinkholes in the study area. In addition, data interpretations from borehole drilling activities and different

391   geophysical approaches were performed in order to reconstruct the Quaternary deposit features, rock head

392   morphology, and karst features. These examples also indicated why multi-disciplinary and complementary

393   data acquisition approaches were necessary in order to ensure accurrate interpretations in mantled karst

394   settings. For this reason, due to the results obtained in this study, the adopted methodological approach

395   could successfully be extended to other areas characterized by similar geological and hydrogeological

396   characteristics.

397   (3) In the study village area, the integration of borehole, geophysical, and hydrogeological data

398   suggested that aquifer pumping had triggered the loss of hydrostatic support and accelerated the

399   washing-out processes. As a result, cover sagging and suffosion sinkholes had been generated in the

400   mantled karst region. Although the groundwater levels had been restored at the time of this study, the

401   sinkholes had the potential to again impact the local residents. Therefore, efforts to investigate and monitor

402   the sinkhole development processes in the region will be required to continue into the immediate future.

403

Acknowledgments

407   DD20190266).

Reference

409   Ahmed, S., Carpenter, P.J., 2003. Geophysical response of filled sinkholes, soil pipes and associated bedrock

410   fractures in thinly mantled karst, east-central Illinois. Environmental Geology 44, 705-716.

411   Al-Halbouni, D., Holohan, E.P., Saberi, L., Alrshdan, H., Sawarieh, A., Closson, D., Walter, T.R., Dahm, T., 2017.

412   Sinkholes, subsidence and subrosion on the eastern shore of the Dead Sea as revealed by a close-range

413   photogrammetric survey. Geomorphology 285, 305-324.

414   Anchuela, O., Pocoví Juan, A., Soriano, M.A., Casas-Sainz, A., 2009. Characterization of karst hazards from the

415   perspective of the doline triangle using GPR — Examples from Central Ebro Basin (Spain). Engineering

416   Geology 108, 225-236.

417   Anikeev, A., 1999. Casual hydrofracturing theory and its application for sinkhole development prediction in the

418   area of Novovoronezh Nuclear Power House-2 (NV NPH-2), Russia, Hydrogeology and engineering geology

419   of sinkholes and karst: 1999, pp. 77-83.

420   Bachrach, R., Mukerji, T., Butler, D., 2005. Analysis of 3D high-resolution shallow seismic and crosswell GPR

421   tomography for aquifer characterization: A case study. Investigations in Geophysics, Near Surface

422   Geophysics: SEG 13, 607-619.

423   Chalikakis, K., Plagnes, V., Guerin, R., Valois, R., Bosch, F.P., 2011. Contribution of geophysical methods to

424   karst-system exploration: an overview. Hydrogeology Journal 19, 1169.

425   Chiabrando, F., Nex, F., Piatti, D., Rinaudo, F., 2011. UAV and RPV systems for photogrammetric surveys in

426   archaeological areas: two tests in the Piedmont region (Italy). Journal of Archaeological Science 38,

427   697-710.

428   Cordua, K.S., Nielsen, L., Looms, M.C., Hansen, T.M., Binley, A., 2009. Quantifying the influence of static-like

429   errors in least-squares-based inversion and sequential simulation of cross-borehole ground penetrating

430   radar data. Journal of Applied Geophysics 68, 71-84.

431   Cueto, M., Olona, J., Fernandez-Viejo, G., Pando, L., López-Fernández, C., 2018. Karst-induced sinkhole

432   detection using an integrated geophysical survey: A case study along the Riyadh Metro Line 3 (Saudi

433   Arabia). Near Surface Geophysics 16, 270-281.

434   Debeglia, N., Bitri, A., Thierry, P., 2006. Karst investigations using microgravity and MASW; Application to

435   Orléans, France. Near Surface Geophysics 4, 215-225.

436   Dinesh, B.V., Nair, G.J., Prasad, A.G.V., Nakkeeran, P.V., Radhakrishna, M.C., 2010. Estimation of sedimentary

437   layer shear wave velocity using micro-tremor H/V ratio measurements for Bangalore city. Soil Dynamics

438   and Earthquake Engineering 30, 1377-1382.

439   Eppelbaum, L., Ezersky, M., Al-Zoubi, A., Goldshmidt, V., Legchenko, A., 2008. Study of the factors affecting the

440   karst volume assessment in the Dead Sea sinkhole problem using microgravity field analysis and 3-D

441   modeling. Advances in Geosciences 19, 97.

442   Fabregat, I., Gutiérrez, F., Roqué, C., Comas, X., Zarroca, M., Carbonel, D., Guerrero, J., Linares, R., 2017.

443   Reconstructing the internal structure and long-term evolution of hazardous sinkholes combining

444   trenching, electrical resistivity imaging (ERI) and ground penetrating radar (GPR). Geomorphology 285,

445   287-304.

446   Frumkin, A., Ezersky, M., Al-Zoubi, A., Akkawi, E., Abueladas, A.-R., 2011. The Dead Sea sinkhole hazard:

447   Geophysical assessment of salt dissolution and collapse. Geomorphology 134, 102-117.

448   Galve, J.P., Castañeda, C., Gutiérrez, F., Herrera, G., 2015. Assessing sinkhole activity in the Ebro Valley mantled

449   evaporite karst using advanced DInSAR. Geomorphology 229, 30-44.

450   Gutiérrez, F., Cooper, A.H., Johnson, K.S., 2007. Identification, prediction, and mitigation of sinkhole hazards in

451   evaporite karst areas. Environmental Geology 53, 1007-1022.

452   Gutiérrez, F., Fabregat, I., Roqué, C., Carbonel, D., Zarroca, M., Linares, R., Yechieli, Y., García-Arnay, Á., Sevil, J.,

453   2019. Sinkholes in hypogene versus epigene karst systems, illustrated with the hypogene gypsum karst of

454   the Sant Miquel de Campmajor Valley, NE Spain. Geomorphology 328, 57-78.

455   Gutiérrez, F., Galve, J., Lucha, P., Bonachea, J., Jordá, L., Jordá, R., 2009. Investigation of a large collapse

456   sinkhole affecting a multi-storey building by means of geophysics and the trenching technique (Zaragoza

457   city, NE Spain). Environmental Geology 58, 1107-1122.

458   Intrieri, E., Gigli, G., Nocentini, M., Lombardi, L., Mugnai, F., Fidolini, F., Casagli, N., 2015. Sinkhole monitoring

459   and early warning: An experimental and successful GB-InSAR application. Geomorphology 241, 304-314.

460   Jiang, X., Lei, M., Zhao, H., 2019. Review of the advanced monitoring technology of groundwater–air pressure

461   (enclosed potentiometric) for karst collapse studies. Environmental Earth Sciences 78, 701.

462   Kaufmann, G., Romanov, D., Tippelt, T., Vienken, T., Werban, U., Dietrich, P., Mai, F., Börner, F., 2018. Mapping

463   and modelling of collapse sinkholes in soluble rock: The Münsterdorf site, northern Germany. Journal of

464   Applied Geophysics 154, 64-80.

465   Kim, J.-H., Park, S.-G., Yi, M.-J., Son, J.-S., Cho, S.-J., 2007. Borehole radar investigations for locating ice ring

466   formed by cryogenic condition in an underground cavern. Journal of Applied Geophysics 62, 204-214.

467   Lee, E.J., Shin, S.Y., Ko, B.C., Chang, C., 2016. Early sinkhole detection using a drone-based thermal camera and

468   image processing. Infrared Physics & Technology 78, 223-232.

469   Lei, M., Gao, Y., Jiang, X., Guan, Z., 2016. Mechanism analysis of sinkhole formation at Maohe village, Liuzhou

470   city, Guangxi province, China. Environmental Earth Sciences 75, 542.

471   Lei, M., Gao, Y., Li, Y., Meng, Y., Yu, L., Gan, F., 2008. Detection and treatment of sinkholes and subsurface voids

472   along Guilin-Yangshuo highway, Guangxi, China, Sinkholes and the Engineering and Environmental

473   Impacts of Karst, pp. 632-639.

474   Maresca, R., Berrino, G., 2016. Investigation of the buried structure of the Volturara Irpina Basin (southern Italy)

475   by microtremor and gravimetric data. Journal of applied geophysics 128, 96-109.

476   Meng, Y., Ji, F., Jia, L., Jiang, X.-z., Lei, M.-t., 2014. A new approach for forecasting the appearance of sinkholes

477   near the Jinshazhou tunnel. Environmental earth sciences 71, 3339-3347.

478   Paine, J.G., Buckley, S.M., Collins, E.W., Wilson, C.R., 2012. Assessing Collapse Risk in Evaporite Sinkhole-prone

479   Areas Using Microgravimetry and Radar InterferometryAssessing Sinkhole Collapse Risk Using

480   Microgravimetry And Radar Interferometry. Journal of Environmental and Engineering Geophysics 17,

481   75-87.

482   Pueyo Anchuela, Ó., Casas Sainz, A.M., Pocoví Juan, A., Gil Garbí, H., 2015. Assessing karst hazards in urbanized

483   areas. Case study and methodological considerations in the mantle karst from Zaragoza city (NE Spain).

484   Engineering Geology 184, 29-42.

485   Ronen, A., Ezersky, M., Beck, A., Gatenio, B., Simhayov, R.B., 2019. Use of GPR method for prediction of

486   sinkholes formation along the Dead Sea Shores, Israel. Geomorphology 328, 28-43.

487   Tan, H., Huang, J., Qi, S., 2012. Application of cross-hole radar tomograph in karst Area. Environmental earth

488   sciences 66, 355-362.

489   Tharp, T.M., 1999. Mechanics of upward propagation of cover-collapse sinkholes. Engineering Geology, 23-33.

490   Tharp, T.M., 2002. Poroelastic analysis of cover-collapse sinkhole formation by piezometric surface drawdown.

491   Environmental Geology, 447-456.

492   Wadas, S.H., Tanner, D.C., Polom, U., Krawczyk, C.M., 2017. Structural analysis of S-wave seismics around an

493   urban sinkhole: evidence of enhanced dissolution in a strike-slip fault zone. Natural Hazards and Earth
494   System Sciences 17, 2335.
495   Xeidakis, G., Torok, A., Skias, S., Kleb, B., 2004. Engineering geological problems associated with karst terrains:
496   their investigation. monitoring, and mitigation and design of engineering structures on karst terrains.
497   Bulletin of the geological Society of Greece 36, 1932-1941.
498   Yeh, M.L., Chou, Y.T., Yang, L.S., 2016. The Evaluation of GPS techniques for UAV-based Photogrammetry in
499   Urban Area. ISPRS - International Archives of the Photogrammetry, Remote Sensing and Spatial
500   Information Sciences XLI-B1, 1079-1084.
501   Zhou, W., Lei, M., 2017. Conceptual site models for sinkhole formation and remediation. Environmental earth
502   sciences 76, 818.
503   Zini, L., Calligaris, C., Forte, E., Petronio, L., Zavagno, E., Boccali, C., Cucchi, F., 2015. A multidisciplinary
504   approach in sinkhole analysis: The Quinis village case study (NE-Italy). Engineering geology 197, 132-144.
505